DOI: 10.48011/asba.v2i1.1608

Proportional-Resonant Controller Applied to DSTATCOM in a Hybrid Hydro-PV Generation System

Gabriel M. Cocco * **Lucas G. Scherer** * **Felipe B. Grigoletto** ** **Robinson F. de Camargo** *

* *Federal University of Santa Maria, Santa Maria, RS (e-mails: maiercocco@gmail.com, lgscherer@gmail.com, robinson.camargo@gmail.com).*
** *Federal University of Pampa, Alegrete, RS (e-mail: grigoletto@gmail.com).*

Abstract: In distribution power generation, hybrid systems play an important role, mainly due its flexibility and reliability. This paper deals with the development of a control strategy for hybrid hydro-PV generation system employing a three-phase three-legs Split-Source Inverter (SSI) like a distribution synchronous static compensator (DSTATCOM). The SSI has the ability to feed ac loads with a boost characteristic. In addition, the proposed control strategy ensures regulation for balanced output ac voltages and load disturbance compensation of self excited induction generator (SEIG) based systems, providing the required active and reactive power. The modeling of the system and the design of the resonant controller are presented in detail. In addition, simulation results are presented to demonstrate the performance of the proposed control strategy.

Keywords: Split-Source Inverter; Photovoltaic System; DSTATCOM; SEIG; Micro-hydro.

1. INTRODUCTION

The distributed generation has been diffused due to their advantages over traditional generation systems, where the use of renewable energy allied with static power converters allows an adequate opperation of the energy microgrids (Han et al., 2017).

Hydro turbines (HT) coupled to induction generators (IG) feeding standalone electric loads need reactive power for the terminal voltage control (Chilipi et al., 2014; Tischer et al., 2017; Scherer et al., 2016; Nehrir et al., 2011). Regarding that, Tischer et al. (2017) presents a control strategy for a generation system able to feed linear and nonlinear balanced loads in standalone operation, composed of induction machine, switchable capacitive bank and three-phase three-legs converter. In Rezkallah et al. (2015) a hybrid system composed by PV, hydro and a storage system with batteries is presented. This system employs a boost dc-dc converter and a three-phase inverter. Furthermore, this system is able to manage the energy surplus by using batteries and resistive loads in order to control the ac grid frequency.

In small PV generation systems, generally two stages of energy conversion are required. The first consists of a boost dc-dc converter, and the second stage consists of an inverter. On the other hand, the interest in converters with reduced number of active components has motivated the development of impedance source converters (ZSI) (Siwakoti et al., 2015). By means an impedance network and additional switching states, these converters have an inversion stage with buck-boost capability. Recently, Abdelhakim et al. (2016) proposed the split-source inverter. This topology employs a conventional three-phase inverter and three additional diodes. Compared to ZSI this converter has reduced voltages on the power switches when it operates with high voltage gains. Furthermore, the SSI does not employ shoot-through states and it presents lower number of passive elements. Abdelhakim et al. (2017) and Borges and Grigoletto (2017) present control strategies for three-phase three-legs split-source inverters.

A control strategy for three-phase four-legs split-source inverters as DSTATCOM was presented in Grigoletto et al. (2019). The main objective of control strategies is to keep the output voltages balanced even in situations with balanced or unbalanced loads. Furthermore, depending on the control characteristics, harmonic distortions of the output voltages can be minimized under nonlinear loads. In this way, Tischer et al. (2017) and Attuati et al. (2019) present proportional-resonant controllers for current loops to mitigate some unwanted harmonics.

Therefore, this paper proposes the control for voltage regulation and unbalanced load disturbance compensation on a PV generation system integrated to a three-legs DSTATCOM for induction generators feeding standalone loads. It is proposed a propotional-resonant (PR) current controller, allowing for the rejection of disturbances on the grid fundamental frequency. For the PV power processing,

⋆ The authors would like to thank INCT-GD, CNPq process nº 306490/2017-0, CAPES process nº 23038.000776/2017-54 and FAPERGS process nº 17/2551-0000517-1.

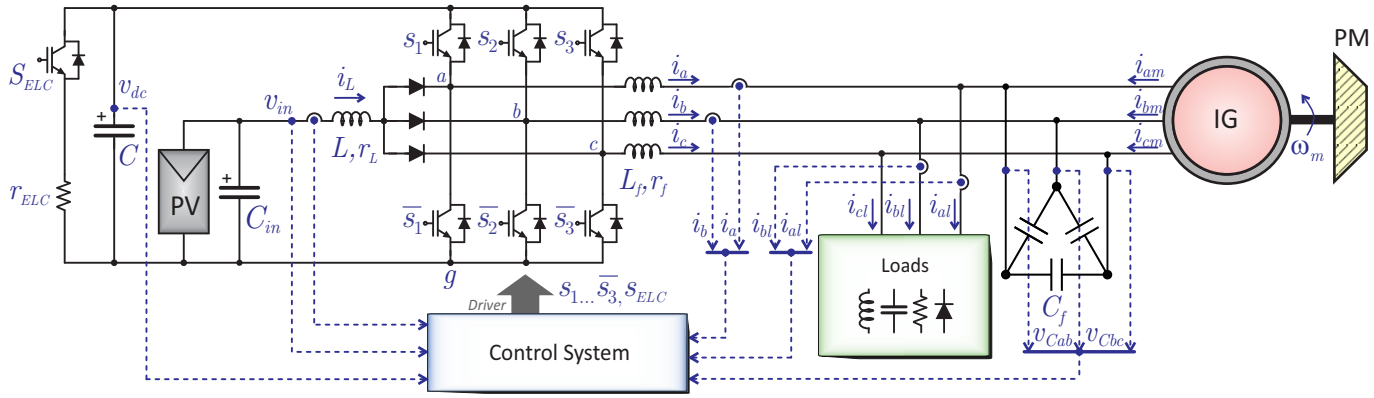

Figure 1. DSTATCOM integrated system with split-source type converter.

a Maximum Power Point Tracking (MPPT) algorithm is designed and employed on the SSI. Analysis, design and simulation of the control system will be presented.

2. DESCRIPTION OF THE HYBRID TOPOLOGY

Figure 1 presents the hybrid hydro-PV power generation system. The split-source inverter employs three-legs with standard complementary power switches and three additional diodes. This converter allows to transfer power from a low voltage input (PV) source to a dc-bus feeding balanced or unbalanced loads at the ac-bus.

2.1 Mathematical modeling of the output and dc stages

The IG is assumed to be in steady-state operation, and its model is the IG equivalent circuit per-phase in steady-state as presented in Figure 2. The equivalent circuit of the IG presents two electrical circuits coupled by a magnetic field, responsible for the transfer of energy from one circuit to the other. The transformation ratio between the coils (stator and rotor) is considered ideal for a conforming induction machine, concluding that $v_r = v_m$ (Simões and Farret, 2014). The rotor circuit is reflected to the stator, making the circuit simplification interesting, and it is not necessary to calculate the magnetization current (i_M) for each speed imposed by the primary machine (PM). Thus, applying the Thévenin theorem to the IG circuit based on the considerations, the IG model impedance is obtained from Figure 2(a), and the equivalent circuit result is represented in Figure 2(b).

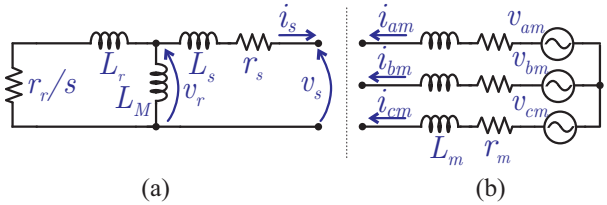

(a) (b)

Figure 2. (a) Per-phase equivalent circuit of the IG. (b) IG simplified three-phase equivalent circuit.

The circuit model of IG is composed of a stator and rotor resistance (r_s, r_r), stator, rotor and mutual inductances (L_s, L_r, L_M), rotor voltage (v_r), and rated slip (s) (Krause et al., 2002). A simplified model, more suitable for control purpose, can be achieved using Thévenin equivalent circuit composed of a sinusoidal voltage source (v_m) and an inductance (L_m) in series with a resistance (r_m). The parameters of the equivalent circuit can be written as:

$$r_m = r_s + (r_r/s)\left(\frac{{L_M}^2}{(r_r/s)^2 + (L_M + L_r)^2}\right), \tag{1}$$

$$L_m = \frac{(r_r/s)^2(L_M + L_s) + {L_M}^2 L_r + L_s(L_M + L_r)^2}{(r_r/s)^2 + (L_M + L_r)^2}. \tag{2}$$

The output stage comprises the three-phase ac-bus of the converter, the output inductors (L_f), the excitation capacitors (C_f) and the induction generator. The capacitor bank C_f provides the reactive power for the induction generator, and the power converter complements the reactive power balance in order to control the ac terminal voltage. The average model in *abc* axes is described by (3)-(5), that is:

$$\begin{bmatrix}\dot{i}_a\\ \dot{i}_b\\ \dot{i}_c\end{bmatrix} = \frac{r_f}{L_f}\begin{bmatrix}-1&0&0\\0&-1&0\\0&0&-1\end{bmatrix}\begin{bmatrix}i_a\\i_b\\i_c\end{bmatrix} + \frac{1}{3L_f}\begin{bmatrix}2&-1&-1\\-1&2&-1\\-1&-1&2\end{bmatrix}\begin{bmatrix}v_{an}-v_{Ca}\\v_{bn}-v_{Cb}\\v_{cn}-v_{Cc}\end{bmatrix} \tag{3}$$

$$\begin{bmatrix}\dot{v}_{Ca}\\ \dot{v}_{Cb}\\ \dot{v}_{Cc}\end{bmatrix} = \frac{1}{Z_l C_f}\begin{bmatrix}-1&0&0\\0&-1&0\\0&0&-1\end{bmatrix}\begin{bmatrix}v_{Ca}\\v_{Cb}\\v_{Cc}\end{bmatrix} + \frac{1}{C_f}\begin{bmatrix}1&0&0\\0&1&0\\0&0&1\end{bmatrix}\begin{bmatrix}i_a+i_{am}\\i_b+i_{bm}\\i_c+i_{cm}\end{bmatrix} \tag{4}$$

$$\begin{bmatrix}\dot{i}_{am}\\ \dot{i}_{bm}\\ \dot{i}_{cm}\end{bmatrix} = \frac{r_m}{L_m}\begin{bmatrix}-1&0&0\\0&-1&0\\0&0&-1\end{bmatrix}\begin{bmatrix}i_{am}\\i_{bm}\\i_{cm}\end{bmatrix} + \frac{1}{3L_m}\begin{bmatrix}2&-1&-1\\-1&2&-1\\-1&-1&2\end{bmatrix}\begin{bmatrix}v_{am}-v_{Ca}\\v_{bm}-v_{Cb}\\v_{cm}-v_{Cc}\end{bmatrix} \tag{5}$$

where i_a, i_b and i_c, are the converter output currents, v_a, v_b and v_c are the output voltages of the converter, v_{Ca}, v_{Cb} and v_{Cc} are the voltages on the capacitors, i_{am}, i_{bm} and i_{cm} are the currents of the induction generator, v_{am}, v_{bm} and v_{cm} are the voltages of the induction generator (back eletromagnetic force) and Z_l is the load impedance. Figure 3 shows the complete average model of the system in *abc* stationary frame. A control strategy can be designed to track sinusoidal references in this frames. However, in order to make the control a regulation problem, the transformation to synchronous frames can be employed.

Now, by representing (3)-(5) in the stationary $\alpha\beta$ frame, to obtain an uncoupled single-phase system, the state-space model (6)-(7) is obtained using the power invariant Clarke transformation. Note that, in three-legs three-phase DSTATCOM, there is no path for the current in the 0 axis. Therefore, the state-space equations can be represented by $\dot{\mathbf{x}}_{\alpha\beta}(t) = \mathbf{A}_{\alpha\beta}\mathbf{x}_{\alpha\beta}(t) + \mathbf{B}_{\alpha\beta}\mathbf{u}_{\alpha\beta}(t) + \mathbf{F}_{\alpha\beta}\mathbf{v}_{\alpha\beta}(t)$ where the

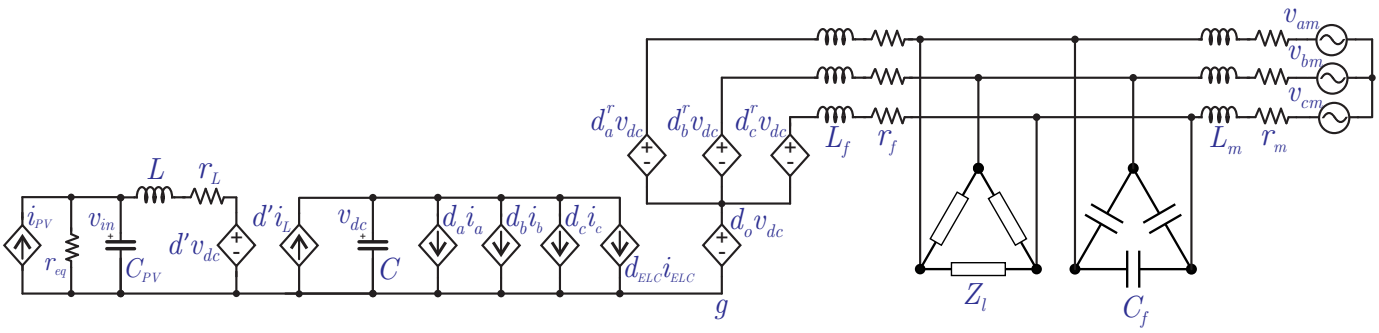

Figure 3. Model of the three-legs SSI DSTATCOM.

states variables are $\mathbf{x}_{\alpha\beta} = \begin{bmatrix} i_\alpha & i_\beta & v_{C\alpha} & v_{C\beta} & i_{\alpha m} & i_{\beta m} \end{bmatrix}^T$, $\mathbf{u}_{\alpha\beta} = \begin{bmatrix} u_\alpha & u_\beta \end{bmatrix}^T$, $\mathbf{v}_{\alpha\beta} = \begin{bmatrix} u_{\alpha m} & u_{\beta m} \end{bmatrix}^T$ and the matrices are given as:

$$\mathbf{A}_{\alpha\beta} = \begin{bmatrix} \frac{-r_f}{L_f} & 0 & \frac{1}{L_f} & 0 & 0 & 0 \\ 0 & \frac{-r_f}{L_f} & 0 & \frac{1}{L_f} & 0 & 0 \\ \frac{1}{C_f} & 0 & \frac{-1}{Z_l C_f} & 0 & \frac{1}{C_f} & 0 \\ 0 & \frac{1}{C_f} & 0 & \frac{-1}{Z_l C_f} & 0 & \frac{1}{C_f} \\ 0 & 0 & \frac{1}{L_m} & 0 & \frac{-r_m}{L_m} & 0 \\ 0 & 0 & 0 & \frac{1}{L_m} & 0 & \frac{-r_m}{L_m} \end{bmatrix}, \tag{6}$$

$$\mathbf{B}_{\alpha\beta} = \begin{bmatrix} \mathbf{I}_{2\times 2}(-1/L_f) \\ \mathbf{0}_{2\times 2} \\ \mathbf{0}_{2\times 2} \end{bmatrix}, \mathbf{F}_{\alpha\beta} = \begin{bmatrix} \mathbf{0}_{2\times 2} \\ \mathbf{0}_{2\times 2} \\ \mathbf{I}_{2\times 2}(-1/L_m) \end{bmatrix}. \tag{7}$$

Thus, the transfer functions that relate the converter output currents to the converter voltages in synchronous frame can be obtained with the transfer function $\mathbf{C}_{\alpha\beta}(s\mathbf{I} - \mathbf{A}_{\alpha\beta})^{-1}\mathbf{B}_{\alpha\beta}$, where $\mathbf{C}_{\alpha\beta} = \begin{bmatrix} 1 & 0 & 0 & 0 & 0 & 0 \end{bmatrix}$ or $\mathbf{C}_{\alpha\beta} = \begin{bmatrix} 0 & 1 & 0 & 0 & 0 & 0 \end{bmatrix}$ and written by:

$$G_{i_{\alpha\beta}, u_{\alpha\beta}}(s) = \frac{i_\alpha(s)}{u_\alpha(s)} = \frac{i_\beta(s)}{u_\beta(s)} = \\ = \frac{C_f L_m Z_l s^2 + \left(L_m + C_f r_m Z_l\right) s + (r_m + Z_l)}{\left\{ \begin{array}{l} C_f L_f L_m Z_l s^3 + \\ + \left[L_f L_m + Z_l C_f \left(L_m r_f + L_f r_m\right)\right] s^2 + \\ + \left[L_f r_m + L_m r_f + Z_l \left(L_f + L_m + C_f r_f r_m\right)\right] s + \\ + Z_l \left(r_f + r_m\right) + r_f r_m \end{array} \right\}}. \tag{8}$$

The transformation of stationary frame *abc* to synchronous frame *dq* (Park transform), can be applied in (3), (4) and (5) resulting in (9), (10) and (11), respectively.

$$\begin{bmatrix} \dot{i}_d \\ \dot{i}_q \end{bmatrix} = \begin{bmatrix} -\frac{r_f}{L_f} & \omega \\ -\omega & -\frac{r_f}{L_f} \end{bmatrix} \begin{bmatrix} i_d \\ i_q \end{bmatrix} + \frac{1}{L_f} \begin{bmatrix} 1 & 0 \\ 0 & 1 \end{bmatrix} \begin{bmatrix} u_d - v_{Cd} \\ u_q - v_{Cq} \end{bmatrix}, \tag{9}$$

$$\begin{bmatrix} \dot{v}_{Cd} \\ \dot{v}_{Cq} \end{bmatrix} = \begin{bmatrix} -\frac{1}{Z_l C_f} & \omega \\ -\omega & -\frac{1}{Z_l C_f} \end{bmatrix} \begin{bmatrix} v_{Cd} \\ v_{Cq} \end{bmatrix} + \frac{1}{C_f} \begin{bmatrix} 1 & 0 \\ 0 & 1 \end{bmatrix} \begin{bmatrix} i_d + i_{dm} \\ i_q + i_{qm} \end{bmatrix}, \tag{10}$$

$$\begin{bmatrix} \dot{i}_{dm} \\ \dot{i}_{qm} \end{bmatrix} = \begin{bmatrix} -\frac{r_m}{L_m} & \omega \\ -\omega & -\frac{r_m}{L_m} \end{bmatrix} \begin{bmatrix} i_{dm} \\ i_{qm} \end{bmatrix} + \frac{1}{L_m} \begin{bmatrix} 1 & 0 \\ 0 & 1 \end{bmatrix} \begin{bmatrix} u_{dm} - v_{Cd} \\ u_{qm} - v_{Cq} \end{bmatrix}. \tag{11}$$

The state space system in the time domain (9)-(11), generically described by $\dot{\mathbf{x}}_{\mathbf{dq}}(t) = \mathbf{A}_{\mathbf{dq}}\mathbf{x}_{\mathbf{dq}}(t) + \mathbf{B}_{\mathbf{dq}}\mathbf{u}_{\mathbf{dq}}(t)$, can be converted into a transfer function by $\mathbf{C}_{\mathbf{dq}}(s\mathbf{I} - \mathbf{A}_{\mathbf{dq}})^{-1}\mathbf{B}_{\mathbf{dq}}$. Thus, the transfer functions that relate the converter output currents to the converter voltages in synchronous frame can be written by:

$$G_{id,iq}(s) = \frac{i_d(s)}{u_d(s)} = \frac{i_q(s)}{u_q(s)} = \frac{L_f s + r_f}{L_f^2 s^2 + 2L_f r_f s + \left(L_f^2 \omega^2 + r_f^2\right)}. \tag{12}$$

The transfer function that relates the direct-axis voltage to the quadrature-axis current is given by:

$$G_{vd}(s) = \frac{v_{Cd}(s)}{i_q(s)} = \frac{-C_f Z_l^2 \omega}{C_f^2 Z_l^2 s^2 + 2C_f Z_l s + C_f^2 Z_l^2 \omega^2 + 1}. \tag{13}$$

For the dc modelling, it can be employed the power balance where the losses can be neglected. Assuming that $v_{qC} = 0$, due to the transformation of stationary to synchronous frame, the power balance equation can be written as:

$$-v_{dc} C \frac{dv_{dc}}{dt} + v_{in} i_L = \frac{\left(v_{dc} U_{ELC}\right)^2}{r_{ELC}} + \left(v_{Cd} i_d + v_{Cq} i_q\right). \tag{14}$$

By applying the Laplace transform in (14), considering the input power portion as a disturbance, and applying a linearization and perturbation technique with $v_{dc}(t) = \tilde{v}_{dc}(t) + V_{dc}$ and $i_d(t) = \tilde{i}_d(t) + I_d$ results in:

$$G_{dc}(s) = \frac{v_{dc}(s)}{i_d(s)} = \frac{-V_d}{C V_{dc} \left(s + \frac{2{U_{ELC}}^2}{C r_{ELC}}\right)}. \tag{15}$$

The control of the converter can be carried out through a multi-loop system composed with PI controllers as discussed in Grigoletto et al. (2019). However, this control strategy can have a unsatisfactory performance with nonlinear large loads which inject harmonics in the system. Thereby, a PR controller for the inner ac current control loops shown in Figure 4 can perform well as the selected harmonics are eliminated, ensuring power quality according with standards (Association et al., 2014).

In this system, there is an outer control loop for the dc bus voltage where the control action is the direct axis reference current. On the other hand, there is a control loop of the magnitude of the ac bus voltage v_{Cd}. The output of this loop is the quadrature axis reference current. The current or voltage control loop for the input inductor i_L or PV capacitor C_{in}, results in a control action to be added with the zero component of the modulation strategy, as described in the next section.

2.2 Description of the modulation strategy

The output voltages of the three-legs converter can be related to the leg voltages by means of (16).

$$\begin{bmatrix} v_{ab} \\ v_{bc} \\ v_0 \end{bmatrix} = \underbrace{\begin{bmatrix} 1 & -1 & 0 \\ 0 & 1 & -1 \\ 1 & 1 & 1 \end{bmatrix}}_{\mathbf{M}_1} \begin{bmatrix} v_{ag} \\ v_{bg} \\ v_{cg} \end{bmatrix}. \tag{16}$$

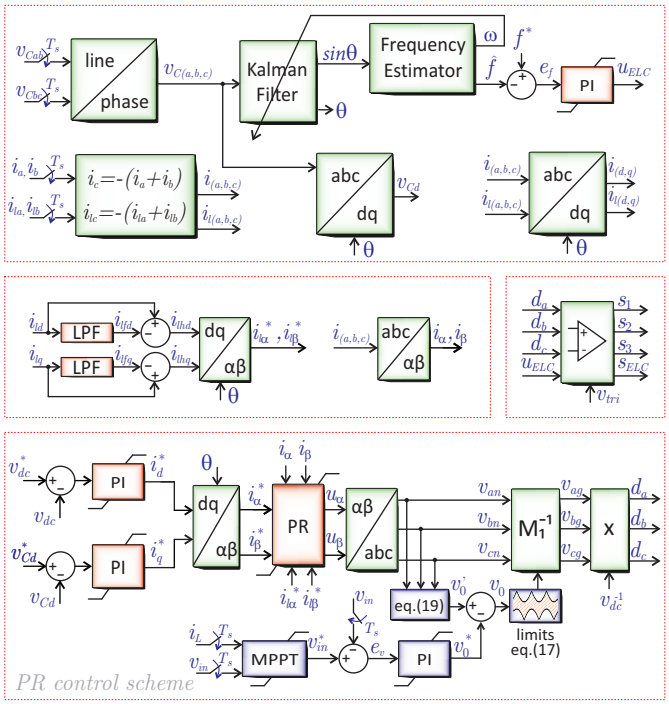

Figure 4. Multi-loop control system for three-legs SSI.

Note that, the variable v_0 is a degree of freedom to be chosen according to a design criteria as dc bus voltage maximization. In order to guarantee the limits of linear operation of the converter, the value of v_0 must be within the limits established by (17), that is:

$$\max\{R_1, R_2, R_3\} \leq v_0 \leq 3v_{dc} + \min\{R_1, R_2, R_3\} \tag{17}$$

where:

$$\begin{aligned} R_1 &= -2v_{an} + v_{bn} + v_{cn} \\ R_2 &= v_{an} - 2v_{bn} + v_{cn} \\ R_3 &= v_{an} + v_{bn} - 2v_{cn} \end{aligned} \tag{18}$$

As demonstrated in Abdelhakim et al. (2016), the choice for v_0, intends to minimize the ripple over the current i_L and the voltage v_{dc}:

$$v_0 = \max\{R_1, R_2, R_3\}. \tag{19}$$

Pre-multiplying both sides of (16) by $\mathbf{M}_1^{-1}$ results in:

$$\begin{bmatrix} v_{ag} \\ v_{bg} \\ v_{cg} \end{bmatrix} = \begin{bmatrix} d_a \\ d_b \\ d_c \end{bmatrix} v_{dc} = \left(\begin{bmatrix} d_a^* \\ d_b^* \\ d_c^* \end{bmatrix} + \begin{bmatrix} \mathbf{1} \end{bmatrix}_{3\times 1} d_0 \right) v_{dc}, \tag{20}$$

where d_a, d_b, d_c, are the duty cycles associated with the switches s_1, s_2 and s_3. d_a^*, d_b^*, d_c^*, are the reference duty cycles, that is:

$$\begin{bmatrix} d_a^* \\ d_b^* \\ d_c^* \end{bmatrix} = \frac{1}{3v_{dc}} \begin{bmatrix} 2 & -1 & -1 \\ -1 & 2 & -1 \\ -1 & -1 & 2 \end{bmatrix} \begin{bmatrix} v_{an} \\ v_{bn} \\ v_{cn} \end{bmatrix}. \tag{21}$$

The drive signals for the switches are obtained by the comparison of the modulating signals with a up-down carrier. In addition, the maximum and minimum operating limits are shown, where $d_{max} = \max\{R_1, R_2, R_3\}/3v_{dc}$, $d_{min} = 1 + \min\{R_1, R_2, R_3\}/3v_{dc}$ e $d_0 = v_0/3v_{dc}$.

2.3 Description of the SSI input stage

When at least one of the lower switches of the converter legs ($\bar{S}_1$, $\bar{S}_2$ ou $\bar{S}_3$) is ON, the inductor L is conected to the input voltage source v_{in} and it accumulates energy, according to Figure 5.a. The dynamic equations which describes the voltage on the inductor, v_L, and the capacitor current, i_C, in this state, with duration t_y, are given by:

$$\frac{di_L}{dt} = -\frac{r_L i_L}{L} + \frac{v_{in}}{L}, \qquad \frac{dv_{dc}}{dt} = -\frac{i_{Lo}}{C}. \tag{22}$$

On the other hand, when the upper legs switches (S_1, S_2 e S_3) are ON, the energy stored in the inductor is transferred to the dc bus capacitor C, according to Figure 5.b. The dynamic equations that describe the voltage on the inductor, v_L, and the capacitor current, i_C, with duration t_x, in this state are given by:

$$\frac{di_L}{dt} = -\frac{r_L i_L}{L} + \frac{v_{in} - v_{dc}}{L}, \qquad \frac{dv_{dc}}{dt} = \frac{i_L - i_{Lo}}{C}. \tag{23}$$

where i_{Lo} is the output current reflected to the dc bus:

$$i_{Lo} = [2s_1 - 1]\, i_a + [2s_2 - 1]\, i_b + [2s_3 - 1]\, i_c. \tag{24}$$

Defining the duty cycle as $D = t_y/(t_x + t_y)$, in steady

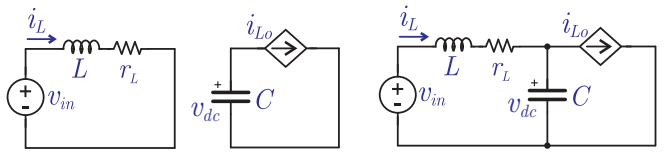

Figure 5. Operation states of the split-source converter: (a) At least one of the switches $\bar{S}_1$, $\bar{S}_2$ or $\bar{S}_3$ is ON, (b) Switches S_1, S_2 and S_3 are ON.

state, where $t_x + t_y = T_s$, the static gain of the input stage can be written as Abdelhakim et al. (2017):

$$\frac{V_{dc}}{V_{in}} = \frac{1}{1-D}, \tag{25}$$

where V_{in} and V_{dc} are respectively the input voltage and the dc bus voltage in steady state.

The average model can be obtained by multiplying (22) by d and (23) by $(1-d)$. On the other hand, the perturbation and linearization method can be employed, where the variables are replaced by a dc variable and a disturbance signal ($d = D + \tilde{d}$). Thus, it can be written (26) as:

$$\begin{aligned} \tilde{i}_L(s) &= \frac{V_{dc}}{Ls + r_L}\tilde{d}(s) - \frac{1-D}{Ls + r_L}\tilde{v}_{dc}(s), \\ \tilde{v}_{dc}(s) &= \frac{1-D}{Cs}\tilde{i}_L(s) - \frac{I_L}{Cs}\tilde{d}(s) - \frac{1}{Cs}\tilde{i}_{Lo}(s). \end{aligned} \tag{26}$$

In (26), the second order terms are neglected, the input voltage is considered constant and i_{Lo} is considered a disturb signal. By assuming a constant dc-bus voltage, the input current transfer function can be simplified resulting in a equation presented and used in Grigoletto et al. (2019) that relates the inductor current and duty cycle.

In order to achieve the maximum power point in a real PV system, the input voltage v_{in} over the capacitor C_{in} can be controlled. In this way, the scheme of SSI stages can represented in Figure 6.

From the circuit of Figure 6, the average model can be described as:

$$\mathbf{A} = D \begin{bmatrix} -r_L/L & 1/L \\ -1/C_{in} & -1/C_{in}r_{eq} \end{bmatrix} + (1-D) \begin{bmatrix} -r_L/L & 1/L \\ -1/C_{in} & -1/C_{in}r_{eq} \end{bmatrix}, \tag{27}$$

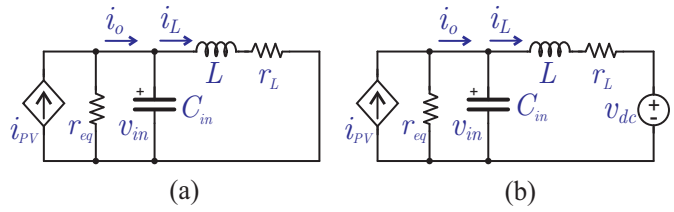

Figure 6. Operation states of the split-source converter: (a) At least one of the switches $\bar{S}_1$, $\bar{S}_2$ or $\bar{S}_3$ are ON, (b) Switches S_1, S_2 and S_3 are ON.

$$\mathbf{B} = D\begin{bmatrix}0 & 0\\ 0 & 1/C_{in}\end{bmatrix} + (1-D)\begin{bmatrix}-1/L & 0\\ 0 & 1/C_{in}\end{bmatrix}. \tag{28}$$

From (27)-(28), the input capacitor voltage $v_{in}(s)$ can be related to the duty cycle $d(s)$ by the transfer function:

$$\frac{v_{in}(s)}{d(s)} = \frac{-V_{dc}r_{eq}}{Lr_{eq}C_{in}s^2 + (L + r_L r_{eq}C_{in})s + (r_{eq} + r_L)}. \tag{29}$$

A PI controller can be employed to control i_L or v_{in}. In addition, the reference current i_L^* or voltage v_{in}^* can be obtained by a Maximum Power Point Tracking (MPPT) algorithm to extract energy from the PV source (Subudhi and Pradhan, 2013).

3. CONTROLLER DESIGN

3.1 Inner ac current loop

The inner current control loop structure is shown in Figure 4. It consists of a PR controller based loop. It is implemented both on the α and β axes, with the tracking of i_α^*, i_β^* and $i_{l\alpha}^*$, $i_{l\beta}^*$, generating the u_α and u_β control actions, respectively.

The PR controller is chosen in this specific application because it is based on the internal model principle, resulting in a good reference tracking and disturbance rejection if the models of the references and disturbances are included in the feedback control loop. As the connection of balanced or unbalanced linear loads consist in a disturbance in the fundamental frequency, the addition of a resonant controller with complex poles tuned to the system frequency will ensure that the references are correctly tracked and the currents remain balanced, even in the presence of unbalanced loads. For this work, it is used the following PR controller equation:

$$C_{PR}(s) = k_{PR}\frac{s^2 + 2\xi_z\omega_z s + {\omega_z}^2}{s^2 + 2\xi_p\omega_n s + {\omega_n}^2}. \tag{30}$$

In this representation, ω_n is the frequency of resonant controller, $0 < \xi_p,\xi_z \leq 1$ is a damping factor, and k_{PR} is the resonant gain. This controller achieves infinite gain in a narrow frequency band around the resonance frequency, which is directly related with the damping factors $0 < \xi_p$ and $\xi_z \leq 1$. On the other hand, the proportional gain k_P determines the dynamics in terms of phase of the bandwidth and gain margin from (31), and it is tuned in a similar way to the PI controller. In the general case, a set of PR controllers can be used to compensate several fixed and known frequencies. This can be achieved by adding more resonant terms in (30). The multiple resonant controllers can be represented as (32).

$$C_{PH}(s) = k_P\frac{\left(s + \omega_{fz}\right)}{\left(s + \omega_{fp}\right)}, \tag{31}$$

$$C_{PR}(s) = \sum_{h=1,5,7,11,\ldots} k_{PR}\frac{s^2 + 2\xi_z\omega_{zh}s + {\omega_{zh}}^2}{s^2 + 2\xi_p h\omega_n s + (h\omega_n)^2}. \tag{32}$$

The resultant frequency response of designed control for the inner current loops with multiple resonant controllers can be seen in Figure 7.

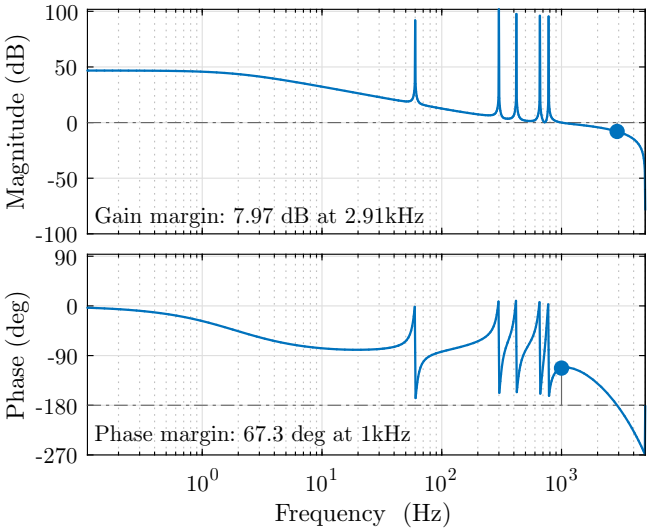

Figure 7. Open loop bode plot of the compensated current control system $C_{PR}(s)C_{PH}(s)G_{i_{\alpha\beta},u_{\alpha\beta}}(s)$.

3.2 Outer voltage loops

Outer loops are employed to the DSTATCOM voltage regulation and SEIG voltage control as shown in Figure 4. As the voltage dynamics are much slower than that of the currents, the inner loops are considered a unitary gain, and for control design purposes the references can be set equal to their actual values, that is, $i_d^* = i_d$ and $i_q^* = i_q$ according to Attuati et al. (2019). The bandwidth of the controllers are designed to be at least a decade below that of the inner current loop. The PI gains obtained are shown in Table 1.

3.3 Frequency control and synchronisation method

An unregulated hydro turbine operating above synchronous speed ($n = 1840$ rpm) is considered as the prime mover, and the frequency control is performed on the demand side by an ELC (Electronic Load Controller). The ELC is composed by an chopper connected to the dc-link of DSTATCOM, as presented in Figure 1. The voltage frequency depends on the balance between input mechanical active power and output active power of the SEIG. Therefore, the power consumed by the system must be maintained constant irrespective of the load variations. The ELC is used to consume the surplus active power generated by the SEIG. The ELC control is based on the estimated PCC (Point of common coupling) terminal voltage frequency, which is performed by a Kalman-based synchronisation method followed by a frequency identification algorithm (Scherer et al., 2016). The PLL

(Phase-Locked Loop) technique can perform poorly due to the uncertainties and distortions in the waveforms, characteristics of isolated systems. The Kalman filter is well known due its ability to deal with linear systems corrupted by uncertainties in the states of the plant as well as measurement noise (Cardoso et al., 2008). The estimated frequency ($\hat{f}$) is then compared with the reference value, which generates a frequency error, $e_f = f^* - \hat{f}$. The error feeds a PI controller which defines the power to be consumed by the ELC (P_{ELC}). The relationship between the power to be consumed by the ELC, and the control action (u_{ELC}) imposed by the element chopper over the r_{ELC} is defined:

$$u_{ELC} = \sqrt{P_{ELC} \cdot r_{ELC}}. \tag{33}$$

The variable u_{ELC} is modulated to generate a PWM signal to be applied to the IGBT switch, GTO or other which drives the r_{ELC}.

4. MPPT ALGORITHM

4.1 Incremental conductance (Inc-Cond) technique

This technique is also considered as a hill climbing method. The MPP can be tracked by comparing the instantaneous conductance I/V to the incremental conductance $\Delta I/\Delta V$. In other words, the solution of Inc-Cond equation (34) is zero at the MPP, positive on the left side of the MPP and negative on the right side of the MPP. The output variable can be the reference value for the panels voltage v_{in}^*.

$$\frac{dP}{dV} = \frac{d(IV)}{dV} = I + V\frac{dI}{dV} \cong I + V\frac{\Delta I}{\Delta V} \tag{34}$$

The incremental conductance algorithm is as efficient and simple as the P&O algorithm, it has good yield under rapidly changing atmospheric conditions. Additionally, a variable step-size can be used to improve the response time, accuracy and performance of the system, but the cost may be higher due to the increased complexity of the control system (Subudhi and Pradhan, 2013).

5. SIMULATION RESULTS

The proposed control loops were simulated from a model performed in Matlab. The system parameters are summarized in Tables 1, 2, 3 and 4.

The parameters shown in Table 2 exposes the sizing of PV system, justifying the behavior of maximum power generation in the simulation results.

5.1 Performance analysis

Figure 8 shows the step response in the dc-link voltage v_{dc}. The reference v_{dc}^* was changed from 500 V to 520 V. Figure 9 shows the step response in the SEIG voltage v_{Cd}. The reference was changed from 220 V to 200 V. The performance of voltage control outer loops were satisfatory.

Figure 10 exposes the performance of variables of interest under a highly nonlinear load step of 4.9 kW. After the load step, the RMS voltage is regulated in a short time.

Table 1. SEIG parameters.

Parameter	**Value**
Nominal power	P_n = 3.7 kW (5 cv)
Line voltage (RMS)	v_s' = 220 V
Nominal rotor speed	n = 1730 rpm
Frequecy	f = 60 Hz
Power factor	FP = 0.81
Excitation capacitor	C_f = 40 μF
Thévenin equivalent	L_m= 2.5 mH, r_m= 0.02 Ω

Table 2. Parameters of PV array system.

Parameter	**Value**
PV array module	SunPower SPR-315E-WHT-D
Max. power ($25°C$-$1kW/m^2$)	P_{MPP} = 2520.6 W
Voltage at MPP	V_{MPP} = 109.4 V
Current at MPP	I_{MPP} = 23.04 A
Series modules per string	N_S = 2
Number of parallel strings	N_P = 4

Table 3. Parameters of DSTATCOM.

Parameter	**Value**
Rated current (RMS)	i_{abc} = 20 A
Dc-link capacitor	C = 4700 μF/900 V
Output filter	L_f= 2.5 mH, r_f= 0.03 Ω
SSI input inductor	L= 5 mH, r_L= 0.03 Ω
PV input capacitor	C_{in}= 10 μF
Switching frequency	f_{sw} = 10 kHz

Table 4. Parameters of controllers.

Controller	**Parameter**	**Value**
v_{dc}, v_d PI	Proportional gain	k_{Pvdc}= -3.74127
		k_{Pvcd}= -0.18418
	Integral gain	k_{Ivdc}= 3.73892
		k_{Ivcd}= 0.18187
i_α, i_β PRD	Damping coefficient	ξ_z = 0.3
		ξ_p = 10^{-6}
	Resonant frequencies (Hz) $\omega_{zh} = h\omega_n = 2\pi f_h$	f_1 = 60
		f_2= 300
		f_3 = 420
		f_4 = 660
		f_5 = 780
	Proportional gain	k_{PR} = 4
		k_P = 1.58602
	Zero and pole of derivative portion (rad/s)	ω_{fp} = 13827.55
		ω_{fz} = 2855.05
v_{in},f PI	Proportional gain	k_{Pvpv}= -0.00265
		k_{Pelc}= -0.1082
	Integral gain	k_{Ivpv}= 0.00264
		k_{Ielc}= 0.10789

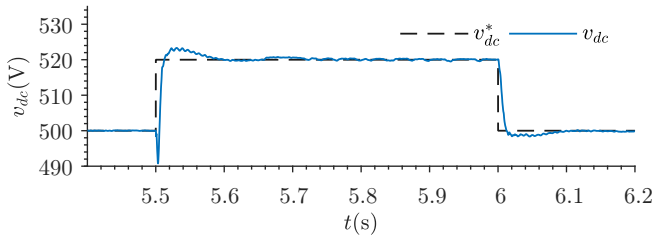

Figure 8. Step response of voltage on DSTATCOM dc-link.

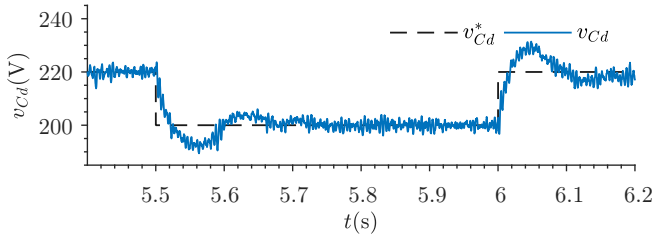

Figure 9. Step response of voltage on SEIG terminals.

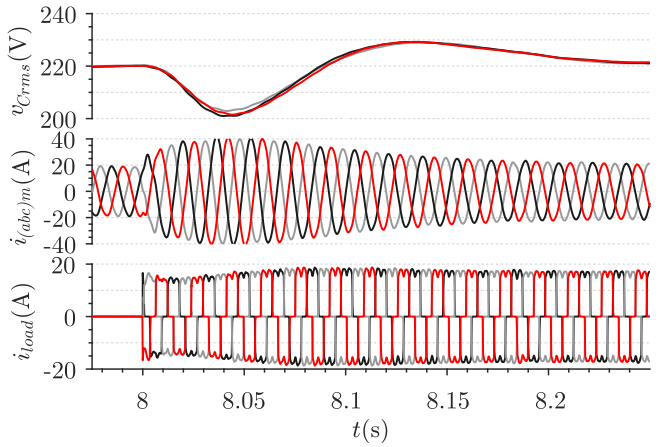

Figure 10. Load step response.

The ELC modulating signal behavior along the simulation is presented in Figure 11. Note that, the ELC power consumption decays abruptly in $t = 8$ s because the compensation is no longer necessary.

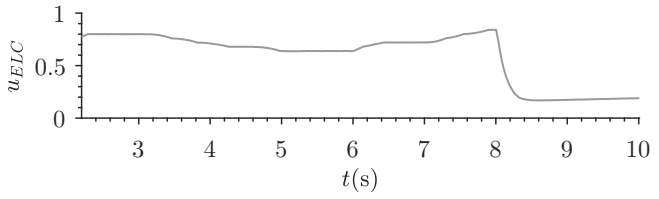

Figure 11. ELC control action response.

An important variable in this system is the frequency regulation. Figure 12 exposes the frequency behavior, together with the input inductor current, and consequently, the PV array current, from the load power step. An adequate accommodation of the system frequency is verified.

The performance of solar energy applied to the system can be seen in the Figure 13. The input variables of the PV system, as irradiation and temperature are represented. It can be observed the influence of input curves on MPP

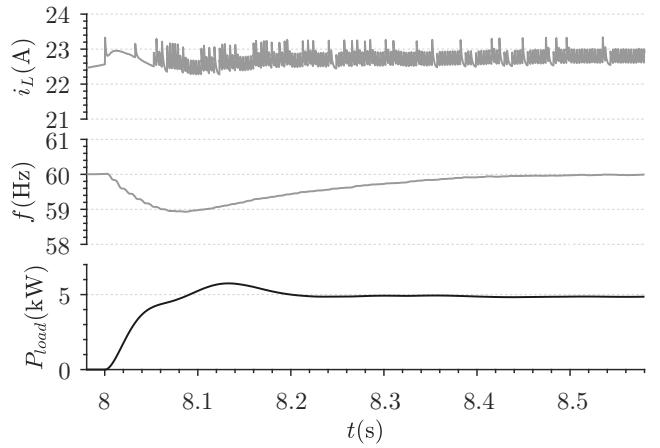

Figure 12. Current on the SSI inductor, ac voltage frequency and load power behavior.

of solar arrays. In adittion, the good performance of the MPPT control algorithm is noted.

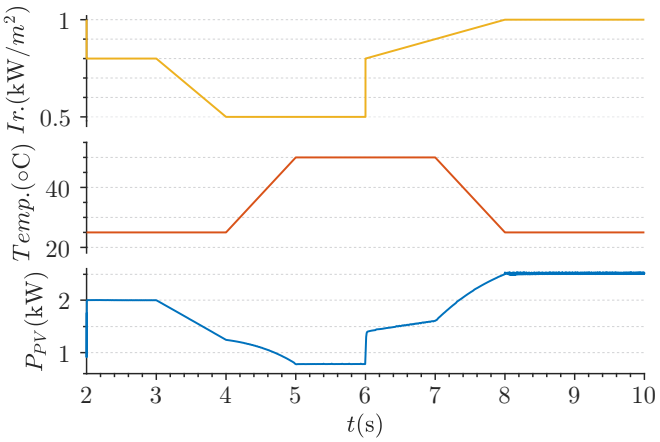

Figure 13. Arbitrary curves for irradiance and temperature on the PV array, and PV system power generation.

A comparison in terms of THD_i resulting from PI and PR loops is performed. The voltage and current harmonics exceeds only the 5_{th} individual harmonic limit, and the THD_i is 8.82%, higher than 5% allowed by standard. On the other hand, in the Figure 14 is represented the performance of PR controller scheme for IEEE 519 standards. Thus, can be observed the conformity with standars in both variables, where several harmonics were canceled.

6. CONCLUSIONS

This paper has proposed a control of an integrated PV generation system with a DSTATCOM for induction generators. The three-legs SSI has the ability to feed three-phase loads, while applying the boost characteristic. In this paper was developed: (i) techniques to design PR controllers that are capable of rejecting voltage disturbances from nonlinear loads connected to the ac bus. (ii) inclusion of additional controlled load ELC to adjust the electrical frequency when there is surplus energy. (iii) inclusion of the photovoltaic panel model and use of a MPPT technique.

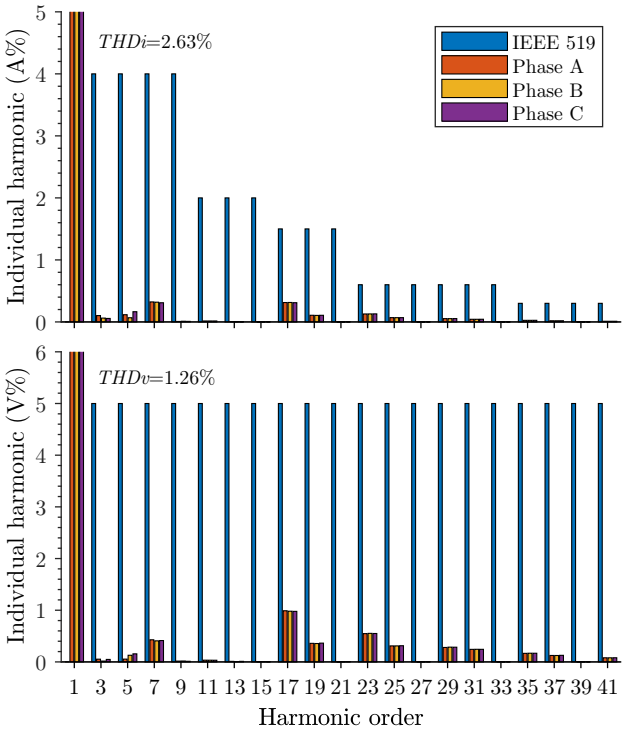

Figure 14. Harmonic spectrum for PR control scheme.

The PR control scheme has good performance in terms of ensuring power quality.

REFERENCES

Abdelhakim, A., Mattavelli, P., Boscaino, V., and Lullo, G. (2017). Decoupled control scheme of grid-connected split-source inverters. *IEEE Transactions on Industrial Electronics*, 64(8), 6202–6211.

Abdelhakim, A., Mattavelli, P., and Spiazzi, G. (2016). Three-phase split-source inverter (SSI): Analysis and modulation. *IEEE Trans. on Power Electron.*, 31(11), 7451–7461.

Association, I.S. et al. (2014). 519-2014-IEEE recommended practices and requirements for harmonic control in electric power systems. *New York, IEEE*.

Attuati, G., de Camargo, R.F., and Scherer, L.G. (2019). Proportional-resonant stator current controller applied to seig based systems. In *2019 IEEE PES Innovative Smart Grid Technologies Conference - Latin America (ISGT Latin America)*, 1–6.

Borges, J. and Grigoletto, F.B. (2017). Finite set model predictive control of grid connected split-source inverters. In *2017 Brazilian Power Electronics Conference (COBEP)*, 1–6.

Cardoso, R., de Camargo, R.F., Pinheiro, H., and Gründling, H.A. (2008). Kalman filter based synchronisation methods. *IET generation, transmission & distribution*, 2(4), 542–555.

Chilipi, R.R., Singh, B., and Murthy, S.S. (2014). Performance of a self-excited induction generator with DSTATCOM-DTC drive-based voltage and frequency controller. *IEEE Transactions on Energy Conversion*, 29(3), 545–557.

Grigoletto, F.B., Cocco, G.M., Scherer, L.G., and de Camargo, R.F. (2019). Control of three-phase four-wire ssi dstatcom integrated to pv generation system. In *2019 IEEE PES Innovative Smart Grid Technologies Conference - Latin America (ISGT Latin America)*, 1–6.

Han, Y., Li, H., Shen, P., Coelho, E.A.A., and Guerrero, J.M. (2017). Review of active and reactive power sharing strategies in hierarchical controlled microgrids. *IEEE Transactions on Power Electronics*, 32(3), 2427–2451.

Krause, P.C., Wasynczuk, O., Sudhoff, S.D., and Pekarek, S. (2002). *Analysis of electric machinery and drive systems*, volume 2. Wiley Online Library.

Nehrir, M.H., Wang, C., Strunz, K., Aki, H., Ramakumar, R., Bing, J., Miao, Z., and Salameh, Z. (2011). A review of hybrid renewable/alternative energy systems for electric power generation: Configurations, control, and applications. *IEEE Transactions on Sustainable Energy*, 2(4), 392–403.

Rezkallah, M., Sharma, S., Chandra, A., and Singh, B. (2015). Hybrid standalone power generation system using hydro-pv-battery for residential green buildings. In *IECON 2015 - 41st Annual Conference of the IEEE Industrial Electronics Society*, 003708–003713.

Scherer, L.G., Tambara, R.V., and de Camargo, R.F. (2016). Voltage and frequency regulation of standalone self-excited induction generator for micro-hydro power generation using discrete-time adaptive control. *IET Renewable Power Generation*, 10(4), 531–540.

Simões, M.G. and Farret, F.A. (2014). *Modeling and analysis with induction generators*. CRC Press.

Siwakoti, Y.P., Peng, F.Z., Blaabjerg, F., Loh, P.C., and Town, G.E. (2015). Impedance-source networks for electric power conversion part i: A topological review. *IEEE Trans. on Power Electro.*, 30(2), 699–716.

Subudhi, B. and Pradhan, R. (2013). A comparative study on maximum power point tracking techniques for photovoltaic power systems. *IEEE Transactions on Sustainable Energy*, 4(1), 89–98.

Tischer, C.B., Tibola, J.R., Scherer, L.G., and de Camargo, R.F. (2017). Proportional-resonant control applied on voltage regulation of standalone SEIG for micro-hydro power generation. *IET Renewable Power Generation*, 11(5), 593–602.